Research Square

Preprints are preliminary reports that have not undergone peer review.
They should not be considered conclusive, used to inform clinical practice,
or referenced by the media as validated information.

Rising seas weaken an offshore sediment lifeline to coastal wetlands

Cédric Fichot

cgfichot@bu.edu

boston university https://orcid.org/0000-0002-1099-5764

Hangjie Lin

boston university

Song Jin

Yantai Institute of Coastal Zone Research, Chinese Academy of Sciences

Sergio Fagherazzi

Boston University https://orcid.org/0000-0002-4048-5968

Article

Keywords:

Posted Date: November 3rd, 2026

DOI: https://doi.org/10.21203/rs.3.rs-11406922/v1

License: This work is licensed under a Creative Commons Attribution 4.0 International License.
Read Full License

Additional Declarations: There is **NO** Competing Interest.

Rising seas weaken an offshore sediment lifeline to coastal wetlands

Hangjie Lin[1], Song Jin[1,2], Sergio Fagherazzi[1], and Cédric G. Fichot[1,*]

[1]Department of Earth and Environment, Boston University, MA, 02215

[2]Yantai Institute of Coastal Zone Research, Chinese Academy of Sciences, Yantai 264003, P. R. China

*Cédric G Fichot

Email: cgfichot@bu.edu

Abstract

Coastal wetlands require sediment to keep pace with rising seas, but sea-level rise may itself weaken their sediment supply. We combine satellite observations, physical sensitivity experiments, and global analyses to reveal this overlooked mechanism. Along coastal Louisiana, winter suspended sediment concentrations declined by 27–58% from 2003 to 2024, coinciding with rising water levels and weakening wave-driven seabed stress, despite stable riverine sediment loading and wave forcing. Sensitivity experiments indicate that deepening alone could reduce sediment-resuspension potential by 31–63% by 2100. Globally, 79% of analyzed coastal waters between 66°S and 66°N exhibit strong wave–sediment coupling. Under SSP5-8.5, projected deepening reduces wave-driven bottom stress near wetlands by 17–23% by 2100. Rising seas can thus increase sediment demand while weakening potential offshore sediment supply.

Main

Coastal wetlands buffer waves and storms, support biodiversity and store substantial amounts of blue carbon[1,2,3]. Yet their persistence under accelerating relative sea-level rise (RSLR) depends critically on whether vertical accretion can keep pace with rising water levels[4-6]. This challenge is compounded by widespread declines in riverine sediment supply. Damming, channel engineering and land-use change in recent decades have sharply reduced riverine sediment delivery to many deltas and estuaries[7,8]. Meanwhile, deep subsidence and compaction of organic-rich Holocene deposits in many low-gradient deltas amplify RSLR across many low-lying coastal plains[9,10]. The combination of increasing sediment demand caused by the growing accommodation space and declining sediment supply is pushing many coastal wetlands towards sediment starvation[5,11,12].

Against this backdrop, sediment stored in shallow coastal waters can provide an important external source for wetland accretion. Waves and currents resuspend sediment from shallow shelves, bays and tidal flats, after which tides, wind-driven circulation and storm surges can transport it landward[13,14]. This marine sediment supply can be particularly important where rivers no longer directly nourish wetland platforms[11,15], and field and modeling studies show that remobilized sediment can sustain substantial, and in some systems, dominate the mineral accretion[16–21]. Resuspension therefore provides a physical mechanism through which sediment stored in shallow offshore waters can be remobilized and delivered to wetlands, helping offset deficits in vertical accretion[16,19,20]. Recycling of eroding marsh edges can also support vertical accretion[22], although it redistributes existing marsh material and can accompany lateral wetland loss[23].

Rising seas, however, also have the potential to weaken this offshore sediment supply. Global wetland assessments commonly emphasize the increase in accommodation space caused by RSLR[4,24,25], but sediment availability is prescribed as an external boundary condition. Although inundation can promote deposition and plant growth[4,26], deepening of nearshore waters can also alter the processes mobilizing sediment. As water depth increases, wave orbital velocities at the seabed decrease, reducing wave-driven bottom shear stress[14,27]. Nearshore deepening can therefore efficiently reduce the resuspension of bed sediment even if surface wave conditions remain unchanged[14,27]. RSLR may consequently impose a previously overlooked double pressure on coastal wetlands by increasing the amount of sediment required to maintain elevation while simultaneously reducing the availability of marine sediment that could meet that demand[11,12]. Projections that assume fixed offshore sediment concentrations or static turbidity conditions may therefore underestimate the vulnerability of sediment-limited wetlands to rising seas[24,25].

Here we test this mechanism first along the Louisiana coast, where rapid RSLR and subsidence coincide with extensive wetland loss and exceptionally rich hydrodynamic and geomorphic observations[10,28,29]. We combine satellite-derived suspended sediment concentrations (SSC) from 2003–2024 with observations of waves, water levels, riverine sediment loads and wetland change to assess whether long-term changes in nearshore sediment availability are consistent with RSLR-driven reductions in wave resuspension. We then explore the potential of this mechanism globally using a Wave–Sediment Coupling Index (WSCI) that identifies coastal waters where SSC variability is strongly

coupled to wave forcing, and quantify the exposure of adjacent coastal wetlands to projected declines in wave-driven bottom stress. Our results identify a mechanism through which rising seas can weaken the offshore sediment supply on which many coastal wetlands depend, adding a dynamic constraint on sediment supply to the increasing accommodation-space demand imposed by RSLR.

Results

Nearshore sediment resuspension declines with RSLR

Monthly nearshore SSC along the Louisiana coast exhibited pronounced spatial and seasonal variability, typically ranging from 5 to 30 mg L^{-1} (**Figure 1a-b, S1**). We divided the coastline along the 4-m isobath into four regions spanning, from west to east, the Chenier plain (Section 1), the Atchafalaya delta (Section 2), the deteriorating Terrebonne delta plain (Section 3), and the coastal zone adjacent to the Mississippi River outflow (Section 4). The Atchafalaya and Mississippi River plumes directly influence SSC in Sections 2 and 4, respectively, while elevated SSC were also observed along the Chenier Plain. In contrast, SSC in Section 3 was consistently lower than in the other regions.

Despite these spatial differences, all four sections exhibited similar seasonal patterns, with consistently higher SSC in winter than in summer, reflecting enhanced sediment resuspension driven by cold fronts and associated wave activity[17,30] (**Figure 1b, S2-S3**). This seasonality closely followed variations in wind and wave forcing rather than riverine sediment loading, particularly along the Chenier and Terrebonne coasts, which are less directly influenced by river plumes (**Figure 1c**). Water levels were also generally lower in winter than in summer (**Figure 1c**), allowing stronger winter waves to interact more effectively with the seabed and enhance sediment resuspension. Seasonal cooling and atmospheric forcing contribute to Gulf Coast water-level variability, while post-frontal northerly winds can further lower coastal water levels through wind-driven set-down[30,31].

Regressions using the monthly climatological data further supported the importance of wave-driven resuspension in controlling nearshore SSC (**Figure S4**). Riverine suspended sediment loading alone explained only 1%, 21%, 0% and 53% of climatological SSC variance in Sections 1-4 (R^2 values of 0.01,0.21, 0 and 0.53), respectively, with the greatest explanatory power adjacent to the Atchafalaya and Mississippi river influence. Including wave-driven bottom shear stress yielded much higher adjusted R^2 values of 0.90,0.92, 0.85 and 0.84, respectively. Analysis of the full monthly records also showed additional explanatory power of wave stress beyond river loading in all four sections, whereas the greatest additional river contribution occurred in Section 4 (**Figure S5**). Thus, riverine inputs and wave-driven mobilization both help regulate nearshore SSC, with their relative importance varying alongshore.

Most importantly, satellite observations revealed a substantial decline in nearshore SSC between 2003 and 2024 (**Figure 2a**). The decline was much more pronounced during winter and in regions less directly influenced by river plumes. Coastwide winter SSC decreased by approximately 0.40 mg L^{-1} yr^{-1}, more than twice the summer decline of ~0.17 mg L^{-1} yr^{-1}. Winter SSC declined most rapidly along the Chenier Plain (Section 1; 0.70 mg L^{-1} yr^{-1}), compared with approximately 0.30 mg L^{-1} yr^{-1} in the river-influenced

Sections 2 and 4 and 0.27 mg L^{-1} yr^{-1} along the Terrebonne Coast (Section 3). The fitted winter SSC reductions were 57.5%, 26.5%, 35.8% and 32.9% for Sections 1–4, respectively. Summer trends were much weaker, reaching only 0.29, 0.12 and 0.06 mg L^{-1} yr^{-1} (40.6%, 21.5%, 16.1%) in Sections 1–3, respectively, with no significant decline detected near the Mississippi River outflow in Section 4 (**Figure 2a**). The faster winter decline narrowed the winter–summer SSC contrast, weakening the seasonal cycle, especially in Section 1.

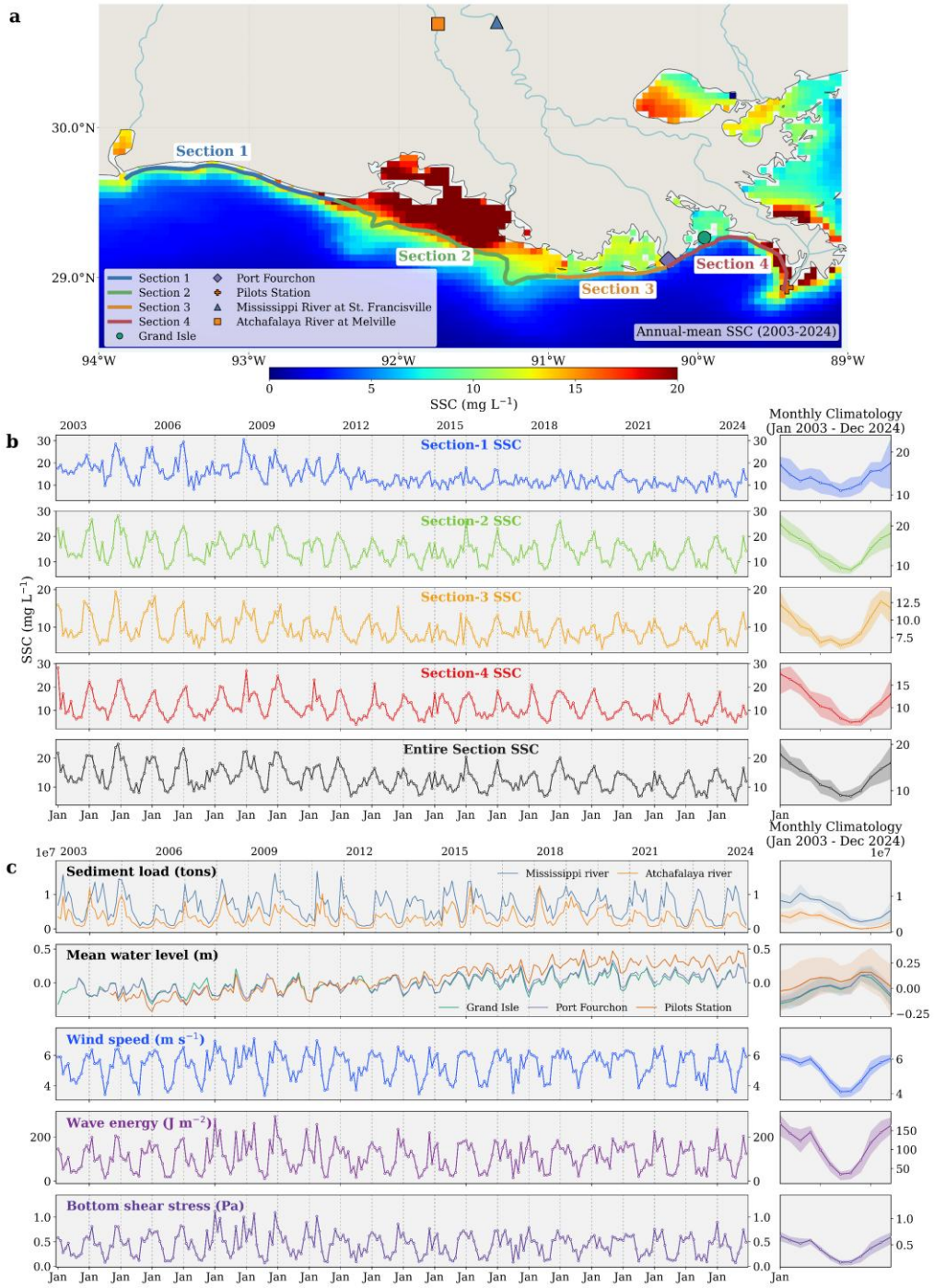


Figure 1 | Spatiotemporal variability in nearshore SSC and environmental forcing along the Louisiana coast. (a) Mean satellite-derived SSC across the Louisiana nearshore zone from 2003 to 2024. Colored lines delineate the four coastal sections analyzed along the 4-m isobath, spanning the Chenier Plain (Section 1), Atchafalaya-influenced coast (Section 2), Terrebonne delta plain (Section 3) and Mississippi River-influenced coast (Section 4). Symbols indicate representative tide gauges and river stations used to characterize water levels and riverine suspended sediment loading. **(b)** Monthly SSC time series from January 2003 to December 2024 for each coastal section and the full Louisiana coastal domain. Right panels show the corresponding monthly climatologies, with shaded envelopes indicating interannual variability. Overall, SSC exhibits a pronounced but weakening seasonal cycle, with winter maxima and summer minima, superimposed on a long-term decline. (**c**) Monthly time series (left) and corresponding climatologies (right) of potential environmental drivers of nearshore SSC, including riverine suspended sediment loading, mean water level, wind speed, wave energy, and wave-driven bottom shear stress.

Riverine sediment loading, wind speed and wave energy did not show a common decline matching the observed SSC trends (**Figure 1c**, **2b**). In contrast, water levels rose in both seasons, whereas wave-driven bottom shear stress declined significantly in winter but showed no significant summer trend. For a given wave height and period, deeper water attenuates near-bed orbital motion and reduces the capacity of waves to exceed sediment-entrainment thresholds. The winter observations are therefore consistent with depth-driven weakening of resuspension, even without a decline in surface wave energy.

The stronger SSC decline in winter compared to summer is consistent with the seasonal dependence of sediment resuspension along the Louisiana coast (**Figure 2**). Frequent cold-front-driven waves during November–February repeatedly mobilize fine bed sediment, making winter SSC particularly sensitive to reductions in bottom shear stress[30]. Lower winter water levels further strengthen wave-bed coupling (**Figure 1c**). Moreover, reduced winter disturbance may also increase the residence time of sediment at the seabed and promote consolidation, progressively increasing the shear-stress threshold required for subsequent erosion[32]. During summer, when wave forcing and vertical mixing are weaker and biological stabilization can increase erosion thresholds[33], SSC may exhibit a lagged reduction in response to the reduced winter sediment mobilization. Such threshold and bed-memory effects provide a possible mechanism by which declining winter resuspension can propagate into subsequent seasons, while producing the substantially stronger SSC trends observed during winter.

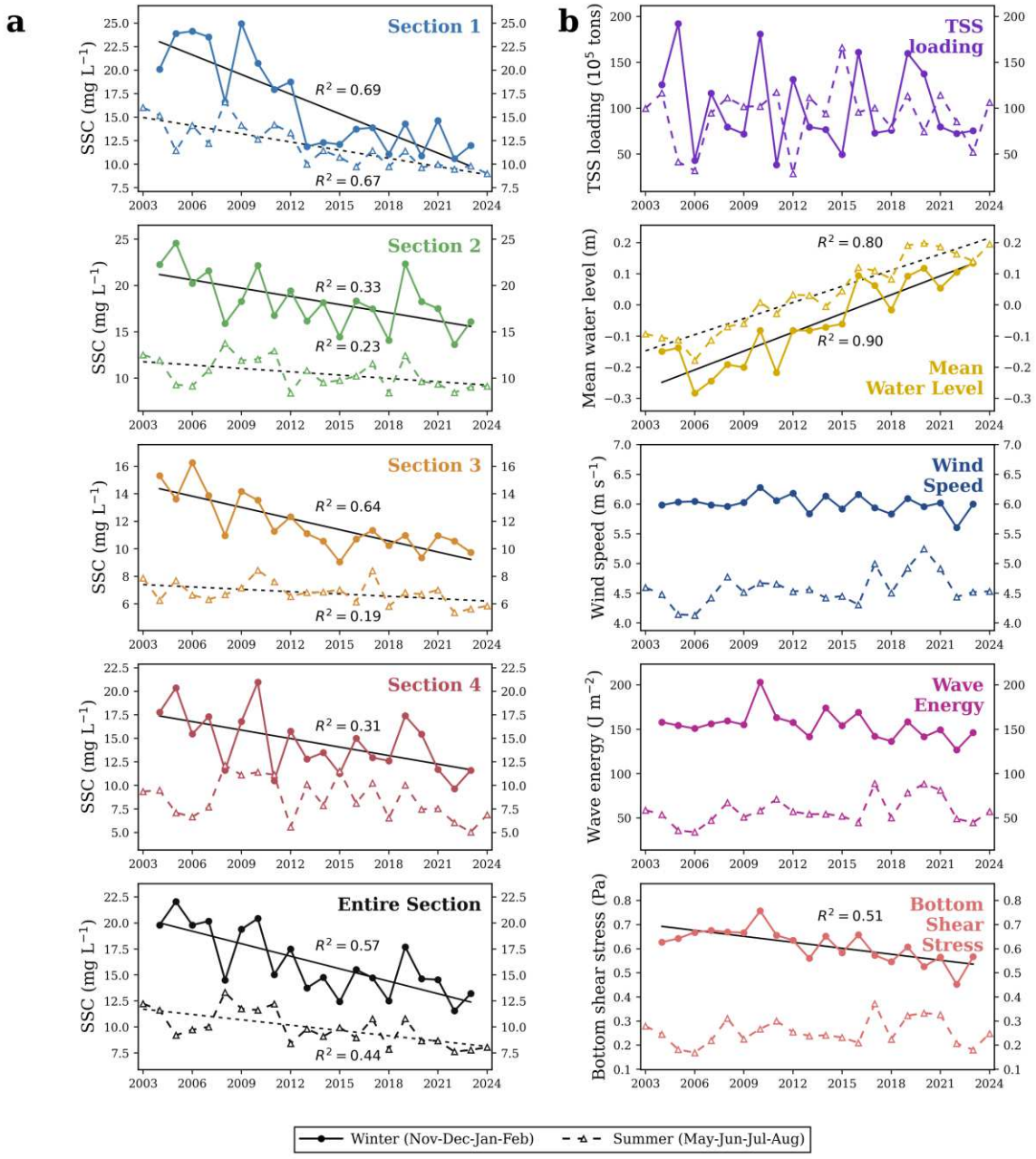


Figure 2 | Seasonal and interannual trends in nearshore SSC and environmental forcing. (a) Annual winter and summer SSC for each of the four coastal sections and the full Louisiana coastal domain from 2003 to 2024. Here, winter is defined as November–February using a cross-year seasonal window, and summer as May–August. Filled circles and solid lines denote winter means; open triangles and dashed lines denote summer means. Black solid and dashed lines show significant fitted winter and summer trends, respectively, with coefficients of determination (R^2). **(b)** Corresponding seasonal and interannual variability in potential drivers of SSC, including riverine suspended sediment loading, mean water level, wind speed, wave energy, and bottom shear stress.

Offshore SSC declines coincide with coastal marsh degradation

Spatial patterns of wetland vertical accretion varied with offshore SSC trends and riverine influence (**Figure 3a-d**). Across more than 200 Coastwide Reference Monitoring System (CRMS) stations, section-median accretion increased from 4.65 mm yr^{-1} in the Chenier Plain to approximately 13 mm yr^{-1} in Sections 3 and 4. The lowest median accretion thus coincided with the strongest winter SSC decline in Section 1. Matching SSC change to the 2006–2015 accretion observation window further yielded a positive relationship across the four sections (**Figure S6**), supporting spatial covariation without separating offshore resuspension from riverine inputs in Sections 2 and 4 or establishing causal attribution.

Accounting for spatial differences in RSLR (**Figure S7**) revealed a more complex pattern of marsh elevation trajectories. Section 4, which is more directly influenced by Mississippi River sediment inputs, exhibited a median accretion surplus of 1.54 mm yr^{-1}, whereas accretion fell below with RSLR in the other three sections (**Figure 3e, f**). Accretion deficits were therefore not confined to areas with limited riverine sediment supply, but occurred across coastal settings with contrasting riverine influence, subsidence rates and hydrodynamic connectivity. This pattern is consistent with marsh sediment availability reflecting not only direct riverine inputs, but also the mobilization and redistribution of sediment stored within the broader coastal system.

Changes in horizontal marsh area showed spatial contrasts alongside long-term offshore SSC trends. All four coastal sections experienced net marsh loss between 2000 and 2019, with the greatest losses occurring in the Chenier plain (Section 1) and Terrebonne delta plain (Section 3), the two sections with the strongest long-term declines in offshore SSC and limited direct riverine sediment supply (**Figure 3g, h**). By contrast, marsh losses were smaller in the Atchafalaya- and Mississippi-influenced sections. The spatial distribution of marsh loss varied with offshore SSC trends and riverine influence.

These relationships do not imply a direct local causal relationship between offshore SSC and marsh change. Sediment mobilized offshore must be transported through shallow coastal waters, bays and tidal channels before reaching vegetated marsh surfaces, and its contribution to vertical accretion depends on hydrodynamic connectivity, local subsidence, vegetation-mediated trapping, and belowground organic matter production. Nevertheless, across the Louisiana coast, independent observations of offshore sediment availability, vertical accretion and marsh-area change show that declining offshore SSC co-occurs with marsh degradation, while differences in accretion balance underscore the importance of local controls.

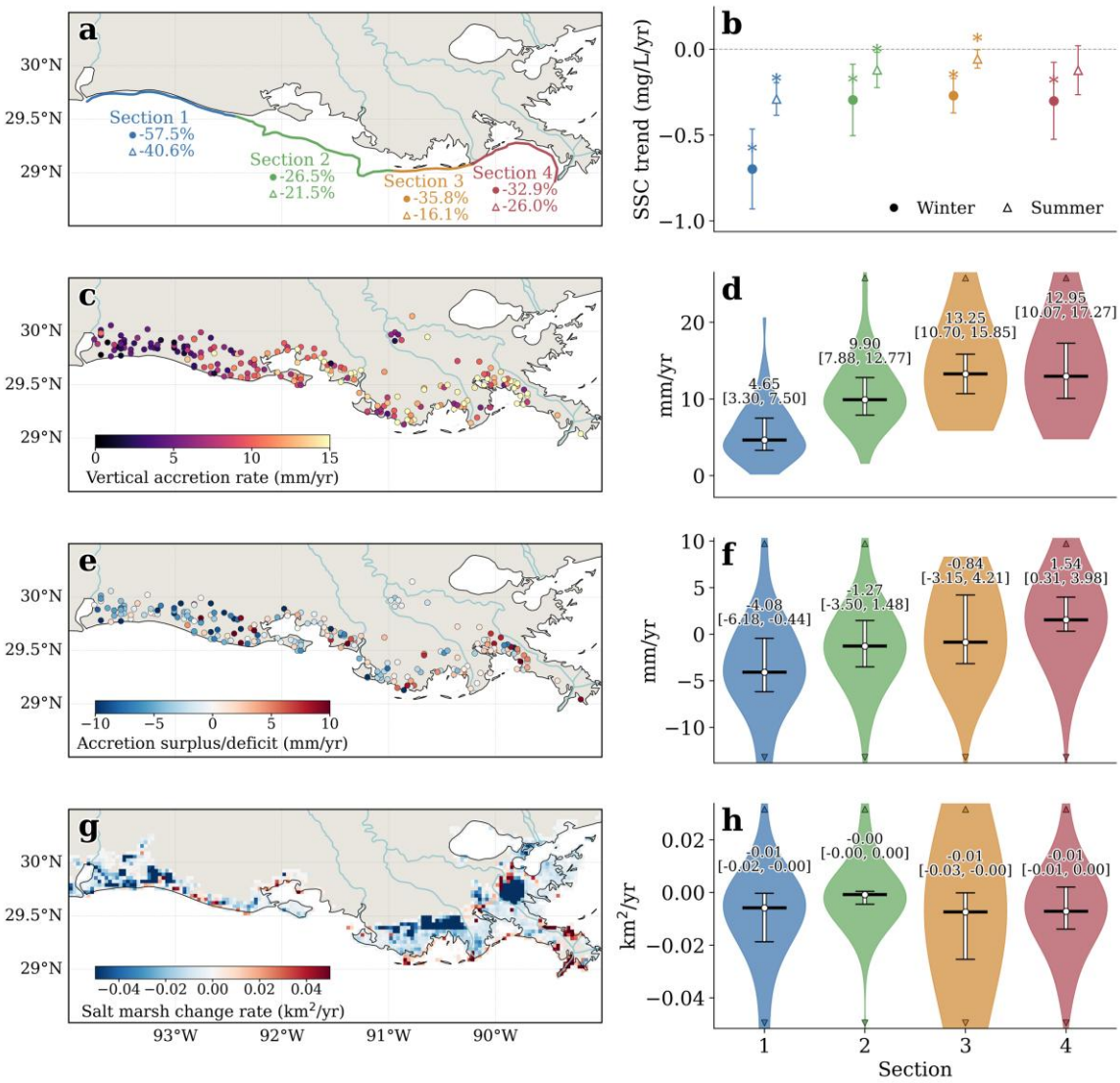


Figure 3 | Spatial covariation of nearshore suspended-sediment trends, marsh vertical accretion, accretion surplus or deficit, and marsh-area change across coastal Louisiana. (a) Locations of the four coastal sections along the 4-m isobath. Values beneath each section indicate the fitted percentage change in suspended sediment concentration (SSC) over the analysis period for winter (filled circles) and summer (open triangles). **(b)** Winter and summer SSC trends for the four coastal sections. Symbols show fitted linear trends and error bars denote 95% confidence intervals; asterisks indicate statistically significant trends ($P < 0.05$). **(c)** Spatial distribution of vertical accretion rates measured at Coastwide Reference Monitoring System (CRMS) stations. **(d)** Distributions of vertical accretion rates within each coastal section. **(e)** Spatial distribution of accretion surplus or deficit relative to local relative sea-level rise (RSLR), with positive values indicating that vertical accretion exceeds RSLR and negative values indicating an accretion deficit. **(f)** Distributions of accretion surplus or deficit within each coastal section. **(g)** Spatial distribution of net salt-marsh area change rates from 2000 to 2019. **(h)** Distributions of

salt-marsh area change rates within each coastal section. In **d, f** and **h**, violin colors correspond to Sections 1–4, white circles and black horizontal markers indicate medians, white vertical bars indicate interquartile ranges, and bracketed values report the 25^{th}–75^{th} percentile interval. Displayed y-axis ranges are restricted to emphasize differences in medians and interquartile ranges; triangles at the plot boundaries indicate observations outside the displayed range.

Rising seas progressively reduce sediment resuspension potential

A water-depth sensitivity analysis reveals how historical and projected RSLR can weaken sediment-resuspension potential along the Louisiana coast (**Figure 4**). Fixed-depth and deepening cases use identical historical wave forcing, with resuspension potential defined by the annual integrated excess of combined wave–current stress above the critical entrainment threshold (**Figure S8**). Across 2003–2024, the modeled loss in annual resuspension potential averaged 7.4%, with the percentage loss calculated relative to the corresponding fixed 4-m case (**Figure 4a, b**). This comparison shows that increasing water depth can reduce sediment-resuspension potential even without a weakening of surface waves, because deeper water weakens wave motion at the seabed.

Extending this depth sensitivity across future RSLR scenarios reveals a progressive amplification of this effect through the end of the century. Assuming linear RSLR rates of 5, 10, 15 and 20 mm yr^{-1}, which span the range of elevated rates relevant to coastal Louisiana (12 ± 8 mm yr^{-1})[10], resuspension potential declines by 31%, 44%, 55% and 63%, respectively, by 2100 relative to the fixed 4-m depth reference (**Figure 4a, b**). The magnitude of the response increases systematically with the rate of RSLR and the direction of weakening persists across the tested critical shear-stress thresholds (**Figure S9a–d**).

This historical and scenario-based sensitivity experiment reveals that, as relative sea level rises and nearshore waters deepen, the capacity of waves to mobilize seabed sediment progressively declines. RSLR may therefore impose a growing sediment supply-demand imbalance on coastal wetlands, simultaneously increasing the sediment required to maintain elevation while reducing the potential for adjacent coastal waters to resuspend sediment available for landward transport.

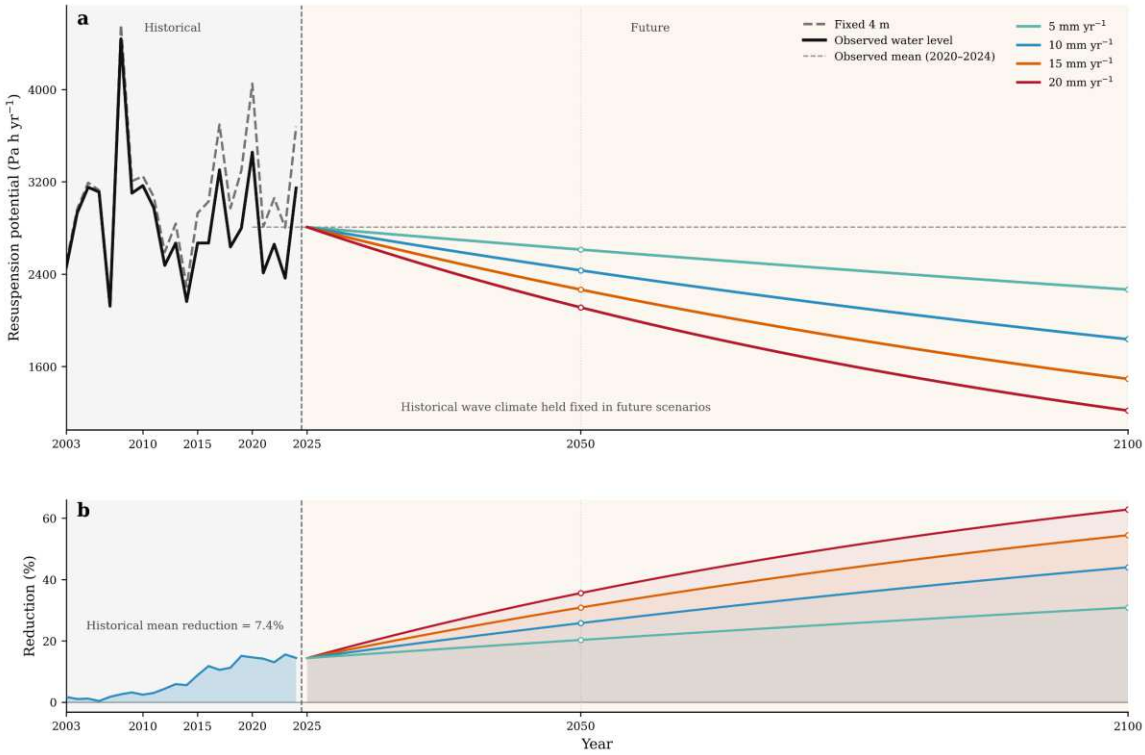


Figure 4 | Historical and projected decline in wave-driven resuspension potential caused by RSLR in coastal Louisiana. (a) Annual resuspension potential, integrated from combined wave–current stress exceeding 0.5 Pa, from the historical period to 2100 for a fixed 4-m reference depth, observed water-level changes, and future RSLR scenarios of 5, 10, 15 and 20 mm yr^{-1}. The horizontal dashed line indicates mean resuspension potential under observed water levels during 2020–2024, and the vertical line separates the historical and projected periods. **(b)** Percentage reduction in resuspension potential relative to the fixed 4-m depth reference. Historical cases use identical annual wave forcing; future curves use a fixed historical wave climate and imposed deepening, showing depth sensitivity rather than interannual forecasts.

Wave-driven sediment resuspension as a global mechanism

This mechanism is not unique to the Louisiana coast. Across many shallow, low-gradient coasts, waves mobilize bed sediment and maintain it in suspension, making it available for potential landward transport. Global patterns in the Wave–Sediment Coupling Index (WSCI) from 2003–2024 identify regions where nearshore SSC is strongly coupled to wave forcing and may therefore be particularly sensitive to RSLR-driven reductions in bottom shear stress (**Figure 5a**). Higher WSCI indicates stronger positive coupling between SSC and significant wave height, and approximately 79% of the valid coastal waters (between 66°N and 66°S) has WSCI ≥ 0.6, used here as a descriptive threshold for strong positive wave-SSC coupling. This pattern is consistent with a widespread role for wave-driven resuspension in nearshore sediment availability. High WSCI remains prevalent when locations north of 66°N are included, although the area fraction falls to approximately 71% (**Figure S10**).

Regional WSCI patterns show spatial coherent contrasts reflecting the relative influences of fluvial sediment supply, tidal dynamics, and wave exposure within specific coastal systems (**Figure 5b**). In Louisiana, the Yukon and the Yellow River Delta, river plumes create distinct low-WSCI zones that transition toward higher WSCI along more wave-exposed open coasts. These patterns are robust across different SSC retrieval approaches (**Figure S11**). Similar landward-to-seaward transitions occur in the funnel-shaped Río de la Plata and Severn estuaries, consistent with stronger fluvial and tidal influences in their inner reaches. Regional differences in sediment supply and coastal exposure further shape these patterns. The sediment-depleted Nile coast, following construction of the Aswan Dam, exhibits high WSCI[34], whereas weak coupling in the Rufiji–Mafia Channel is consistent with sheltering by offshore islands[35]. Strong coupling also characterizes the western abandoned delta along the Ganges–Brahmaputra–Meghna coast and the exposed southern Gulf of Carpentaria. At a broader scale, mean WSCI generally decreases with increasing riverine sediment flux (**Figure S12**). Together, these patterns demonstrate that WSCI captures spatial variations in the relative importance of sediment supply, tidal influence, and wave exposure in shaping coastal sediment dynamics[14].

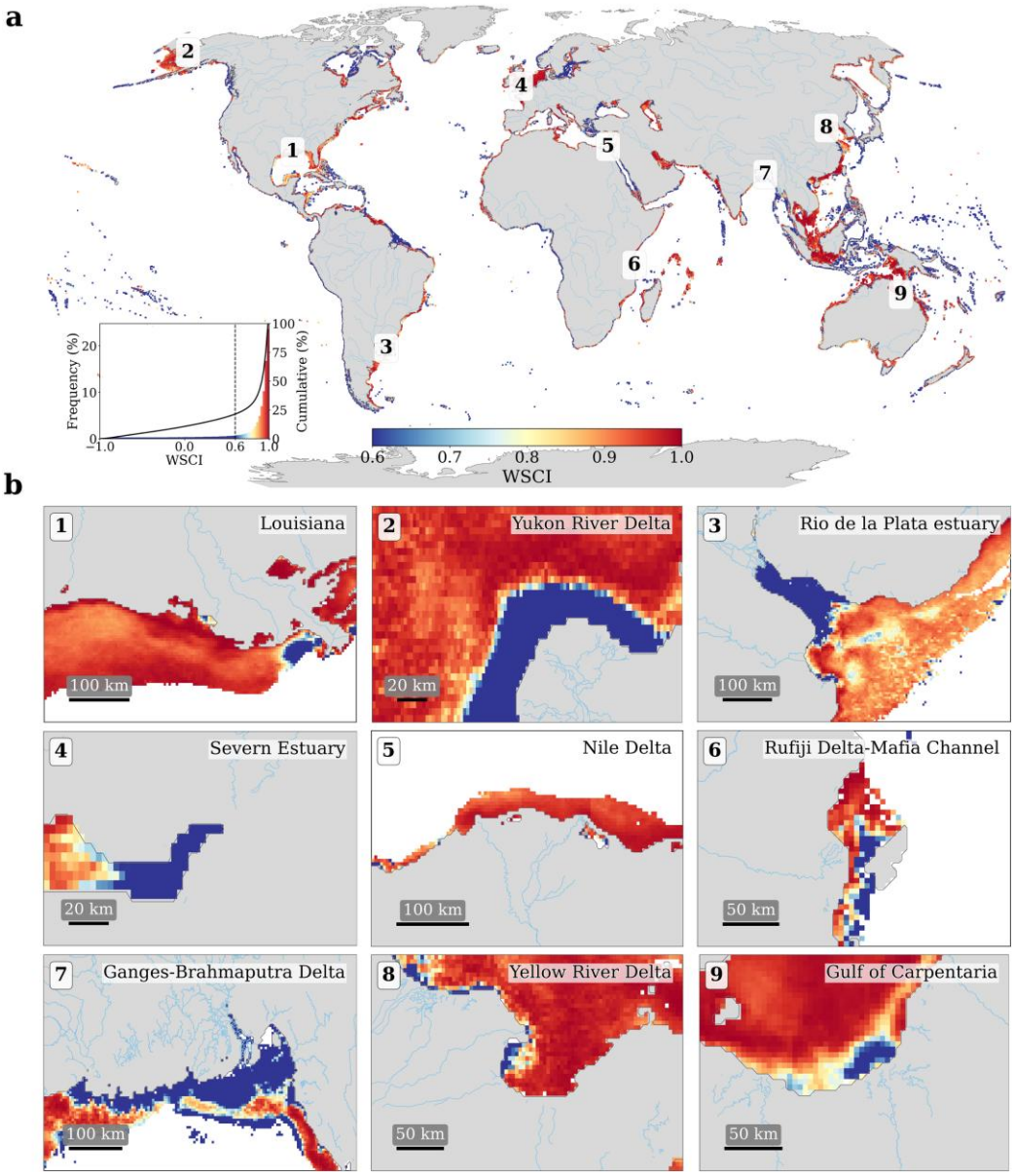


Figure 5 | Global patterns of wave-SSC coupling. (**a**) Global distribution of the Wave–Sediment Coupling Index (WSCI) from 2003 to 2024, restricted to latitudes ≤66°N. Higher WSCI indicates stronger positive coupling between SSC and significant wave height. The inset shows the frequency and cumulative distribution of WSCI, with a WSCI of 0.6 marking the threshold associated with significant positive wave–SSC coupling. Numbered boxes indicate the locations of the regional examples shown in (b). (**b**) Regional distributions of WSCI across nine representative coastal systems: (1) Louisiana, (2) Yukon River Delta, (3) Río de la Plata estuary, (4) Severn Estuary, (5) Nile Delta, (6) Rufiji Delta–Mafia Channel, (7) Ganges–Brahmaputra–Meghna Delta, (8) Yellow River Delta and (9) southern Gulf of Carpentaria. These examples span contrasting river-, tide- and wave-influenced environments and illustrate the strong spatial heterogeneity in wave control on nearshore SSC.

Rising seas weaken bottom shear stress near coastal wetlands globally

Combining AR6 RSLR projections[36,37] with the global distribution of strongly wave-coupled coastal waters identified by WSCI reveals widespread weakening of wave-driven sediment resuspension in shallow waters adjacent to coastal wetlands (**Figure 6a**). Under SSP5-8.5, rising sea levels are projected to reduce wave-driven bottom shear stress (τ_{wave}) by approximately 17–23% across different wetland types by 2100 across coastal waters connected to different wetland types. These projections isolate the effect of increasing water depth while holding wave conditions constant, thereby quantifying the direct influence of RSLR on wave-driven bottom stress.

The magnitude and spatial extent of this weakening differ among wetland types. Mean τ_{wave} declines by ~23% for salt marshes, compared with 21% for mangroves and 17% for tidal flats. Salt marshes also experience a greater proportion of severe bottom shear-stress reductions (**Figure 6b**). However, mangroves and tidal flats have greater stress-weighted wetland area, calculated as linked wetland area weighted by fractional stress decline, reaching 4.1×10^4 and 3.6×10^4 km², respectively, compared with 1.7×10^4 km^2 for salt marshes (**Figure 6c**). Among wetland areas linked to declining offshore stress, approximately 44% of the distance-weighted salt-marsh area is associated with reductions exceeding 25%, compared with 35% for mangroves and 27% for tidal flats (**Figure S13**). This threshold is comparable to the projected reduction in bottom shear stress along coastal Louisiana, providing a regional benchmark for interpreting the global patterns.

These global patterns are robust across analytical assumptions and become more pronounced over time and under higher-emission scenarios. Salt marshes consistently exhibit the greatest mean decline in τ_{wave} and the largest proportion of exposure exceeding the 25% benchmark across alternative assumptions about wetland–offshore connectivity (**Figure S14**). Under all SSPs, projected weakening is substantially greater in 2100 than in 2050, with higher emissions amplifying both mean stress reductions and stress-weighted wetland area (**Figure S15**). Differences among scenarios are relatively small in 2050 for the proportion of exposure exceeding 25%, but become more pronounced by 2100. Under SSP5-8.5, stress-weighted wetland area in 2100 reaches approximately 3.4–3.9 times its 2050 value. Excluding regions north of 66°N preserves the relative ranking among wetland types while reducing stress-weighted wetland area, particularly for tidal flats (**Figure S16**). These results extend the mechanism identified along coastal Louisiana to the global scale, demonstrating that continued RSLR will progressively weaken wave-driven bottom stress and reduce the potential for sediment resuspension in shallow coastal waters connected to wetlands.

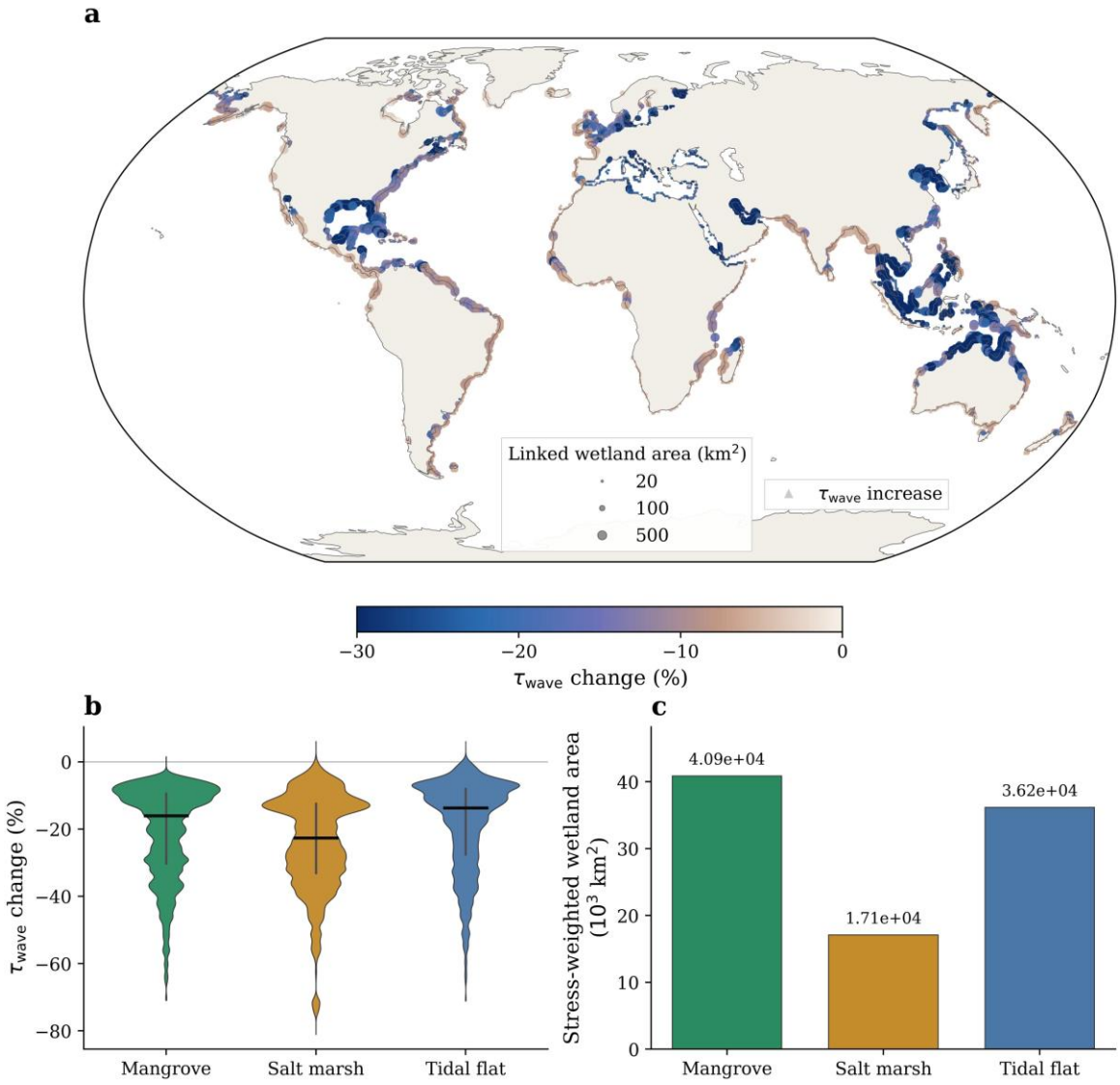


Figure 6 | Global coastal-habitat exposure to projected weakening of wave-driven bottom shear stress. (a) Global distribution of projected changes in wave-driven bottom shear stress (τ_{wave}) in strongly wave-coupled coastal waters near mangroves, salt marshes and tidal flats. Declines are shown by the main color scale, increases by gray triangles, and symbol size represents the distance-weighted area of nearby coastal habitats. **(b)** Distributions of projected offshore τ_{wave} declines for the three habitat types, weighted by nearby habitat area and restricted to locations experiencing declining stress. **(c)** Stress-weighted wetland area (km²) for each habitat type, calculated by weighting linked habitat area by fractional offshore stress decline. Locations with increasing bed stress contribute zero to this metric. Habitat–offshore associations are defined using a distance-decay kernel (50 km e-folding distance; 150 km maximum distance; see Methods). All panels show the median projection for 2100 under SSP5-8.5, including vertical land motion, with locations north of 66°N excluded.

Discussion

An overlooked global vulnerability of coastal wetlands to sea-level rise

Coastal-wetland vulnerability to RSLR is commonly framed as an accommodation-space problem. As sea level rises, wetlands must accumulate sediment and organic matter rapidly enough to maintain their elevation, while seawalls, urban development and steep topography can restrict landward migration and produce coastal squeeze[4,24,25]. This framework captures the increasing sediment demand imposed by RSLR, but generally treats sediment availability as an external boundary condition rather than as a process that can itself respond to rising water levels[4,5,24,25]. Here, our results reveal that by increasing water depth and weakening wave–driven bottom shear stress, RSLR can simultaneously increase the sediment required to maintain wetland elevation while reducing the capacity of adjacent coastal waters to mobilize sediment for landward transport. Rising seas may therefore impose a dual pressure on coastal wetlands.

Louisiana provides evidence that this mechanism is already operating. The state contains ~40% of the coastal wetlands in the conterminous United States but has experienced a disproportionate share of recent national wetland loss[10,29]. The widespread decline in nearshore SSC documented here is not accompanied by comparable declines in riverine sediment loading or surface wave forcing, but coincides with rising water levels and declining wave-driven bottom shear stress (**Figure 1-2**). Sensitivity experiments further show that increasing water depth alone is sufficient to progressively reduce bottom shear stress and sediment-resuspension potential under unchanged wave conditions (**Figure 4**). With coastal RSLR rates of approximately 12 ± 8 mm yr^{-1} Louisiana provides an early analogue for the depth-driven weakening of sediment resuspension that other low-gradient coasts could increasingly experience as sea level rises[10,28,29].

Our global analysis indicates that this vulnerability extends well beyond Louisiana. Strong wave–SSC coupling characterizes ~79% of the coastal-water area analyzed (**Figure 5**). Under SSP5-8.5, projected mean reductions in wave-driven bottom shear stress near mangroves, salt marshes and tidal flats reach 17–23% by 2100 in strongly wave-coupled waters (**Figure 6**). Marine sediment can sustain wetland accretion[16,19], making this weakening particularly consequential where riverine sediment delivery is declining[7,8]. Global assessments that hold SSC fixed[24,25] therefore risk overstating the mineral-accretion benefit of greater inundation[4,26]. This feedback depends on sediment carried by floodwaters, so it can weaken as deepening reduces the sediment available for deposition. Although future sediment availability will also depend on changes in wave climate and sediment delivery, including storm-driven import, continued RSLR imposes a progressively stronger depth-related constraint on resuspension[18,21,38]. Accounting for sediment availability in shallow offshore waters will therefore be essential for identifying wetlands that are more vulnerable than assessments with fixed sediment supply suggest.

Securing an offshore sediment lifeline to coastal wetlands

Coastal-wetland protection and nature-based adaptation have traditionally emphasized vegetation restoration, tidal connectivity, shoreline stabilization, river diversions and preservation of landward migration space[1,3,15,25]. While these strategies remain essential,

our findings highlight the importance of considering the broader sediment system that sustains wetland elevation. In regions where wave-driven resuspension contributes to nearshore sediment availability (high-WSCI regions), rising sea levels may progressively weaken the mobilization of seabed sediments that can subsequently be transported into tidal channels and onto wetland platforms. Maintaining tidal connectivity alone may therefore be insufficient if the offshore sediment sediment supply becomes increasingly difficult to mobilize.

Effective adaptation may therefore require extending wetland management beyond the wetland edge to encompass the offshore sediment sources and transport pathways that sustain wetland accretion. Shallow sediment reservoirs, wave-driven resuspension zones, and the tidal pathways connecting them to wetlands should be considered interconnected components of the same coastal sediment system[13,15,16]. Identifying and protecting these sediment pathways, while exploring opportunities to enhance sediment availability and delivery, could complement existing restoration strategies as rising seas progressively weaken natural resuspension. Ultimately, safeguarding coastal wetlands against sea-level rise may require not only preserving the space for wetlands to persist and migrate landward, but also sustaining the offshore sediment lifelines that enable them to build vertically.

Methods

Remote-sensing retrieval and validation of suspended sediment concentration

We developed a regionally calibrated empirical algorithm to retrieve suspended sediment concentration (SSC) from satellite remote-sensing reflectance (*Rrs*) at 665 nm over the Louisiana coastal shelf. Field hyperspectral reflectance measurements were collected using a Satlantic HyperPro-II profiler (2009–2010 dataset) or a Spectral Evolution PSR-1100f spectroradiometer (2021 dataset), as described in detail previously[39]. Hyperspectral *Rrs*(λ) measurements were used to extract $R_{rs}(665)$ corresponding to the red band of the satellite ocean-color product, while concurrently collected water samples provided in situ SSC measurements for algorithm calibration. The 665 nm band was selected because red reflectance is sensitive to suspended particle concentrations in optically complex coastal waters and is less affected by chromophoric dissolved organic matter and phytoplankton absorption than shorter visible wavelengths[40]. Given the complex optical conditions of Louisiana coastal waters, influenced by river plumes, shallow-water sediment resuspension, and wetland–shelf exchange, we adopted a field-calibrated regional algorithm rather than a generic global SSC product to improve retrieval accuracy.

The relationship between $R_{rs}(665)$and in situ SSC was determined using a quadratic polynomial fit. The final retrieval equation was

$$SSC = 33620\, R_{rs}(665)^2 + 1473\, R_{rs}(665) + 0.00425$$

where SSC is expressed in mg L^{-1} and $R_{rs}(665)$ in sr^{-1}. The quadratic term accounts for the nonlinear increase in red-band reflectance under higher-turbidity conditions. The calibration used 67 field observations spanning the major nearshore sediment gradients of the Louisiana shelf, and the fitted relationship explained most of the observed SSC variability ($R^2 = 0.975$, **Figure S1a, c**). This result indicates that $R_{rs}(665)$ provides a robust first-order predictor of SSC in this region.

Algorithm performance was evaluated using an independent satellite-*in situ* match-up dataset. To reduce temporal mismatch associated with tides, wave-driven resuspension and rapidly evolving river plumes, we retained only observations for which the *in situ* sampling time and satellite acquisition time differed by no more than ±3 h. For each valid match-up, satellite $R_{rs}(665)$ was converted to remotely sensed SSC using the polynomial above and compared with the corresponding in situ SSC measurement. The matchup showed strong correspondence between remotely sensed and in situ SSC ($y = 0.824x + 0.087$, $R^2 = 0.929$, RMSE = 1.561 mg L^{-1}, $N = 36$, **Figure S1b, d**), demonstrating that the regional algorithm preserved both the concentration gradient and the absolute magnitude of SSC across independent samples.

After calibration and validation, the algorithm was applied to monthly Ocean Colour CCI $R_{rs}(665)$ data[41] to produce mean SSC fields for the Louisiana coastal shelf for following analysis. Monthly $R_{rs}(665)$ observations were first converted to SSC using the same polynomial, and multi-year seasonal means were then calculated for spring (March–May), summer (June–August), autumn (September–November) and winter (December–February). This workflow provides a consistent remote-sensing basis for subsequent

analyses of SSC seasonality, long-term change and wave-driven resuspension. Satellite sampling coverage was characterized using monthly counts of valid daily observations, summarized as pixel-level calendar-month climatologies and section-level time series (**Figure S2–S3**).

Environmental forcing time series and trend analysis

We constructed monthly time series of wind, wave, water-level and fluvial sediment forcing to diagnose the environmental controls on suspended sediment concentration (SSC) variability along the Louisiana coastal shelf. The coast was divided into four sections along the 4 m isobath, from west to east representing the chenier plain, the Atchafalaya River's prograding deltaic sector, the degraded Terrebonne Bay deltaic plain, and the nearshore zone adjacent to the Mississippi River delta. The 4 m isobath was selected because it lies close to the coastal sediment-exchange corridor while remaining offshore of the bays, reducing land-adjacency and potential bottom-reflectance contamination relative to pixels closer to shore. This section framework therefore preserves geomorphic meaning while allowing SSC, wave-driven resuspension and fluvial sediment supply to be compared under a consistent nearshore-depth reference.

Wind and wave forcing were derived from hourly ERA5 reanalysis fields[42]. ERA5 is the fifth-generation ECMWF/Copernicus global reanalysis product and provides hourly estimates of atmospheric, ocean-wave and land-surface variables; here, 10 m wind speed was used as the wind-forcing metric, while significant wave height H_s and mean wave period T were used to estimate wave energy and wave-induced bed shear stress. For each coastal section, hourly wind and wave variables were first spatially averaged and then aggregated to monthly means. The hourly wave records were retained for stress and resuspension-potential calculations; monthly means summarize the resulting forcing time series.

Wave energy per unit horizontal area was estimated from linear wave theory as

$$E = \frac{1}{16}\rho_w g H_s^2$$

where E is wave energy density in J m^{-2}, ρ_w is seawater density, g is gravitational acceleration and $H_s$is significant wave height. Wave-induced bed shear stress was calculated from near-bed wave orbital velocity, with monthly water-level anomalies used to adjust the effective water depth. For month m, the effective depth was defined as

$$h_m = h_0 + \eta_m$$

where $h_0 = 4$ m is the reference depth and η_m is the regional mean water-level anomaly relative to the long-term mean. Positive water-level anomalies increase effective depth and weaken wave orbital motion at the bed, whereas negative anomalies have the opposite effect. For each hourly wave observation, angular frequency was calculated as

$$\omega = \frac{2\pi}{T}$$

and wave number k was obtained from the linear dispersion relation

$$\omega^2 = gk\tanh(kh_m)$$

The near-bed orbital velocity was then estimated as

$$U_b = \frac{\pi H_s}{T\sinh(kh_m)}$$

The orbital excursion amplitude was calculated as

$$A_b = \frac{U_b}{\omega}$$

The wave friction factor was estimated using a rough-turbulent wave-boundary-layer formulation:

$$f_w = 1.39\left(\frac{A_b}{z_0}\right)^{-0.52}$$

where $z_0$is the bed roughness length. When expressed using the Nikuradse equivalent roughness k_s, with $z_0 = k_s/30$, this becomes

$$f_w = 0.237\left(\frac{A_b}{k_s}\right)^{-0.52}$$

Wave-induced maximum bed shear stress was then computed as

$$\tau_w = \frac{1}{2}\rho_w f_w U_b^2$$

This quantity represents wave-only bed shear stress, rather than total bed stress including tidal currents, river currents or wave–current interactions. The formulation explicitly propagates the combined effects of wave height, wave period, water-level anomaly and bed roughness into the estimated resuspension forcing, following the rough-turbulent wave-friction framework used in Soulsby-type bed-shear calculations[27].

Coastal water levels were obtained from NOAA CO-OPS tide-gauge observations at Grand Isle (8761724), Port Fourchon, Belle Pass (8762075), and Pilots Station East, S.W. Pass (8760922). These three stations constrain regional water-level variability across the central-eastern Louisiana coast, the Terrebonne–Barataria coastal sector and the Mississippi River delta front, respectively. Station-level water levels were converted to monthly means, and a regional mean anomaly was then calculated to adjust the 4 m reference depth and evaluate how background water-level variability modulates wave-induced bed shear stress.

Fluvial sediment forcing was represented by WRTDS-derived monthly sediment loads. WRTDS, or Weighted Regressions on Time, Discharge and Season, is a locally weighted regression approach that models concentration or flux as a function of time, discharge and seasonal phase, and is widely used for estimating long-term water-quality trends and riverine material loads[43]. We used sediment-load estimates from the Mississippi River at

St. Francisville and the Atchafalaya River at Melville, representing the two dominant fluvial sediment-supply pathways to the Louisiana shelf. The monthly loads from the two rivers were summed to define regional total TSS loading.

In addition to long-term time-series analysis, we used monthly climatological regressions to evaluate how different forcing combinations explain the seasonal structure of SSC. For each coastal section, 12-month climatologies were calculated for SSC, riverine TSS loading and wave-induced bed shear stress. We then fitted two regression models. The first used riverine TSS loading alone to predict monthly climatological SSC:

$$SSC_m = \alpha + \beta L_m + \varepsilon_m$$

whereas the second included both riverine TSS loading and wave-induced bed shear stress:

$$SSC_m = \alpha + \beta L_m + \gamma \tau_{w,m} + \varepsilon_m$$

Here SSC_m, L_m and $\tau_{w,m}$ denote the multi-year mean SSC, riverine sediment loading and wave-induced bed shear stress for month m. The single-predictor model tests whether fluvial supply alone can reproduce the SSC seasonal cycle, whereas the two-predictor model evaluates whether adding wave-driven resuspension improves the prediction of monthly climatological SSC. These climatological fits summarize seasonality rather than independent month-to-month prediction. Model performance was evaluated using R^2, adjusted $R^2$and RMSE in the observed-versus-predicted monthly climatology diagnostic.

We used the original monthly records from 2003–2024 and retained their seasonal variability. For each coastal section, we fitted three ordinary least-squares models: SSC as a function of river TSS loading alone, wave-driven bottom shear stress alone, and both predictors together. The additional explanatory power of wave stress was quantified as $\Delta R^2_{\text{wave}} = R^2_{\text{river+wave}} - R^2_{\text{river}}$, with the additional river contribution calculated analogously as $\Delta R^2_{\text{river}} = R^2_{\text{river+wave}} - R^2_{\text{wave}}$. Uncertainty was estimated using 2,000 whole-year bootstrap resamples, preserving the within-year seasonal structure (**Figure S5**). R^2 increments require the same complete-case months in all models. They describe conditional associations retaining seasonality, rather than isolated causal effects.

All forcing variables were organized as monthly time series and aligned with the section-level SSC records. Seasonal trend analyses were conducted only for winter and summer to isolate the two most dynamically distinct regimes on the Louisiana shelf. Winter was defined across calendar years, such that winter year Yincludes November–December of year $Y-1$and January–February of year Y; summer was defined as May–August within the same calendar year. At least two valid monthly values were required to compute a seasonal mean, and incomplete edge years were excluded from the cross-year winter analysis.

For each SSC section and each environmental forcing factor, winter and summer trends were estimated separately using ordinary least-squares regression:

$$X_y = \alpha + \beta y + \varepsilon_y$$

where $X_y$is the seasonal mean in year y, and $\beta$is the linear trend slope, expressed as the rate of change per year. Nominal trend significance was assessed from the $p$value of the fitted slope, with $p < 0.05$ used as the threshold for statistical significance; R^2 was also reported to quantify the fraction of interannual variability explained by the linear trend. By placing SSC, sediment loading, water level, wind speed, wave energy and wave-induced bed shear stress within a common seasonal framework, this analysis distinguishes long-term changes from seasonal dynamics and compares the timing and direction of SSC and environmental trends.

Section-based comparison of accretion balance and salt-marsh change

To assess whether nearshore sedimentary conditions are consistent with marsh vertical maintenance and areal change, we used the same four Louisiana coastal sections defined in the environmental-forcing analysis. The section framework previously provided a common nearshore-depth reference for comparing SSC, wave-driven resuspension and fluvial sediment supply. Here, the same framework was extended to vertical accretion, relative sea-level rise and net salt-marsh area change, allowing nearshore sediment conditions and onshore wetland responses to be compared within the same geomorphic units.

This section-based comparison was treated as a first-order spatial approximation linking offshore sediment dynamics to onshore marsh response. In low-gradient deltaic coasts, the pathway by which offshore suspended sediment is transported through tidal channels, bays, shoals, storm-driven flows and vegetated marsh margins to a specific elevation-monitoring point or marsh patch cannot generally be traced uniquely at regional scale. A point-to-point offshore–onshore sediment connection would require high-resolution hydrodynamic–sediment transport modelling and would still be strongly conditioned by local channel connectivity, storms, engineering structures and vegetation-edge migration. We therefore did not assume that each onshore observation was controlled by a single offshore pixel. Instead, each section was interpreted as an alongshore sedimentary–geomorphic unit, and the relevant variables were summarized as distributions across the nearshore-to-marsh transectal domain of that section. This approach preserves the dominant alongshore geomorphic gradient while avoiding over-precise assumptions about local sediment pathways that cannot be directly verified.

The difference between vertical accretion and relative sea-level rise was used as a diagnostic of marsh accretion balance. Vertical accretion and relative sea-level rise were interpreted following the Louisiana coastal wetland vulnerability framework of Jankowski et al.[10], who used CRMS rod surface-elevation table–marker horizon observations to estimate surface-elevation change, vertical accretion, shallow subsidence and relative sea-level rise. In this framework, marsh persistence depends not on absolute sea-level rise alone, but on whether the marsh surface gains sufficient elevation relative to the local water-level reference frame. A marsh site is therefore considered to have an accretion surplus when vertical accretion exceeds relative sea-level rise, and an accretion deficit when vertical accretion is lower than relative sea-level rise.

Relative sea-level rise was interpreted as the vertical water-level pressure experienced by the marsh surface, rather than as a simple tide-gauge trend. Relative sea-level rise

combines shallow subsidence, deeper subsidence and the regional rate of sea-level rise in the Gulf of Mexico[10]. Shallow subsidence is inferred from the difference between vertical accretion and surface-elevation change, deeper subsidence is constrained by regional geologic and geodetic information, and both components are combined with modern sea-level rise. This marsh-surface RSLR is used for accretion balance and does not measure offshore seabed deepening. This definition is particularly important in coastal Louisiana, where substantial subsidence occurs beneath the marsh surface and tide-gauge records alone do not fully represent the vertical change experienced by the marsh platform.

Within each section, vertical accretion, relative sea-level rise and their difference were summarized as transect-scale distributions rather than as single mean values. Each elevation-monitoring observation was associated with its corresponding coastal section, and section-level distributions were calculated for vertical accretion, RSLR and accretion surplus/deficit. These distributions represent the spatial variability of marsh vertical state across the nearshore-to-marsh domain of each section, including the median condition, interquartile range and distributional tails. This distributional treatment is better suited to coastal Louisiana than a single section mean, because the same geomorphic unit may contain rapidly accreting sites, rapidly subsiding sites and vertically deficient sites, reflecting local combinations of sediment delivery, vegetation productivity, shallow compaction and hydrodynamic exposure.

Salt-marsh change rate was defined as the mean annual rate of net area change within each 1/30° grid cell from 2000 to 2019. This variable was derived from the global salt-marsh change dataset of Campbell et al.[44], which used Landsat 5, 7 and 8 imagery in Google Earth Engine to compare an NDVI baseline from 1984–1999 with NDVI anomalies across four five-year epochs between 2000 and 2019. Their method identified salt-marsh loss, gain and recovery using image-quality filtering, peak-biomass seasonal windows, multi-year compositing, temporal-consistency constraints and spatial-connectivity constraints, thereby reducing the influence of individual scenes, tidal-stage variability, seasonality and Landsat 7 scan-line artefacts on marsh-change detection[44].

Aggregating 30 m salt-marsh change information to the 1/30° global tidal grid provides a balance between robust net-change estimation and preservation of coastal spatial detail. The native 30 m change maps capture local marsh-edge erosion, expansion and recovery, but direct pixel-scale coupling to environmental drivers can be sensitive to geolocation uncertainty, patch geometry and local noise. The 1/30° grid provides an intermediate scale: it is fine enough to retain contrasts among adjacent geomorphic settings such as the chenier plain, Atchafalaya, Terrebonne Bay and the Mississippi River nearshore, while being large enough to compute a meaningful balance of salt-marsh loss and gain within each cell. For each grid cell, total net salt-marsh area change from 2000 to 2019 was summed and annualized to $km^2\ yr^{-1}$, yielding a dynamic response variable that can be compared with vertical accretion, RSLR and nearshore sediment-forcing gradients.

Depth control on wave-driven resuspension potential

We used a depth-centred physical diagnostic to test whether relative water-level rise can weaken nearshore wave-driven resuspension. This analysis was not designed to replace a full three-dimensional hydrodynamic and sediment-transport model. Instead, it isolated a

basic mechanism: under the same wave conditions, deeper water reduces near-bed wave orbital motion, thereby lowering bottom shear stress and sediment resuspension potential. The diagnostic used the same hourly ERA5 wave forcing and NOAA CO-OPS water-level observations as the environmental-forcing analysis.

Water-level change was expressed as an effective depth increase relative to an early baseline, rather than as a positive or negative anomaly around the full-record mean. This early-baseline diagnostic isolates long-term deepening; the centred anomalies used for the forcing time series above serve a different purpose. We used 4 m as the reference depth and constructed fixed-depth and observed-water-level cases. The fixed-depth case provides the counterfactual baseline without long-term deepening. The observed-water-level case estimates the effect of actual depth change during 2003–2024.

The depth sensitivity of bottom stress was first evaluated under controlled wave conditions. Holding wave period and bed roughness treatment constant, we examined how wave-induced bottom stress responds to combinations of significant wave height and water depth. The purpose of this step was not to restate the bed-stress formulation, but to quantify the key physical effect: for the same surface wave climate, increasing depth reduces the fraction of wave momentum that reaches the bed. This depth response provides the physical basis for the annual resuspension-potential calculation.

Because the seabed is forced by both waves and currents, the annual resuspension-potential index (RPI) was calculated from combined wave–current bottom stress. The current term was treated as a transparent sensitivity component and represented by an idealized tidal-current signal. When depth changed, current speed was scaled using an approximate constant-transport assumption. Combined bottom stress was calculated using a nonlinear wave–current framework rather than by simply adding wave-only and current-only stresses, because wave and current boundary layers interact[27].

Resuspension potential was defined as the annual positive excess of combined bottom stress above a critical entrainment threshold. For each hourly time step, only the part of combined bottom stress exceeding the critical shear stress was retained and integrated over the year:

$$\mathrm{RPI} = \sum_{t} \max(\tau_{cw,t} - \tau_{cr}, 0)\Delta t$$

RPI therefore records more than whether resuspension occurs; it also reflects how strongly and how persistently the threshold is exceeded. The main analysis used $\tau_{cr} = 0.5$ Pa as a representative threshold, with 0.1 and 0.3 Pa used as sensitivity cases to test whether the result depends on more easily erodible bed conditions.

Historical RPI loss was quantified by comparing the fixed-depth counterfactual with the observed-water-level case. For each year from 2003 to 2024, we calculated RPI under fixed 4 m depth and under the observed-water-level increase. The difference between these two cases represents the reduction in resuspension potential caused by actual deepening under the same wave climate. This comparison separates the effect of water-depth increase from interannual variability in wave forcing, allowing the result to be interpreted as a depth-driven weakening of bed momentum input.

Future RPI was estimated from a depth-response function rather than from assumed changes in future wave climate. We first used the additional-deepening cases to relate added water depth to RPI. We then mapped linear relative sea-level-rise trajectories from 2025 to 2100 onto this response function. The future calculation holds the historical wave climate fixed, so it should be interpreted as a controlled sensitivity experiment: if wave conditions remain unchanged, continued deepening alone reduces wave-driven resuspension potential. This design avoids mixing the depth effect with uncertain future changes in wave climate.

Wave–Sediment Coupling Index

We developed a Wave–Sediment Coupling Index (WSCI) to identify coastal waters where SSC increases systematically with wave forcing. The index summarizes the mean SSC response across the sampled wave-height distribution. For each coastal pixel, daily GlobColour suspended particulate matter (SPM) from the GlobColour merged ocean-colour products[45] and ERA5 significant wave height H_s were paired over 2003–2024; SPM was used as a satellite proxy for SSC, while ERA5 provides significant wave height at hourly resolution. The paired records were sorted into 10 quantile bins according to H_s, and the mean $H_s$and mean SPM were calculated within each bin. WSCI was then defined as the Pearson correlation coefficient between the two binned-mean series. A high WSCI indicates that suspended sediment tends to increase under higher-wave conditions; coupling was considered significant when $p < 0.05$, corresponding to a correlation coefficient of approximately 0.6 for 10 bins. The primary global analysis was restricted to latitudes $\leqslant 66^\circ$ N and compared with the full valid domain (**Figure S10**). Over Louisiana, WSCI was also recalculated from Ocean Colour CCI using the local and Nechad SSC algorithms with the same ERA5 forcing and 10-bin procedure (**Figure S11**).

Importantly, the broad spatial pattern of WSCI over Louisiana is reproduced across GlobColour SPM, the locally calibrated Ocean Colour CCI SSC retrieval and the Nechad algorithm (**Figure S11**), indicating limited sensitivity to the choice of SSC product or retrieval method. This robustness is partly expected because WSCI is correlation-based: constant positive multiplicative or additive calibration offsets do not alter the Pearson correlation. GlobColour is therefore used here to identify spatial patterns of wave–SSC coupling rather than globally calibrated SSC magnitudes or trends, which require regional validation and temporal stability. Binning suppresses within-bin variability, so a high WSCI does not imply high daily predictive skill or establish causality. Nonlinear retrieval errors, changing sensor mixtures, seasonal sampling and common seasonal forcing can also affect the index.

WSCI empirically separates coasts where waves can mobilize bed sediment from coasts where SSC is dominated by other controls. High-WSCI regions indicate a systematic increase in suspended sediment under stronger waves, consistent with an important contribution from wave-driven bed resuspension. These regions are therefore more likely to be affected by water-depth increases associated with sea-level rise: under the same wave climate, deeper water weakens near-bed orbital motion, lowers bottom shear stress and reduces resuspension potential. Low WSCI does not imply that sediment is unimportant. It may instead reflect river-plume dominance, strong tidal control, sea-ice

effects, retrieval uncertainty, limited erodible sediment availability or other local processes. WSCI therefore serves as a global screening metric for identifying coastal waters where suspended sediment is most likely to respond through the wave–bed-resuspension pathway.

We then linked WSCI to global river sediment fluxes to test how fluvial sediment supply modulates wave–sediment coupling. River sediment fluxes were taken from the global major-river dataset of Dethier et al.[8], which estimated suspended sediment flux and its human-driven changes for 414 major rivers using satellite imagery and in situ records. For each river, we extracted the WSCI value from the nearest coastal grid cell and also calculated a regional mean within a 0.25° radius around that point to reduce pixel-scale noise and estuary-location uncertainty. Rivers were then grouped by sediment-flux order of magnitude, and the mean WSCI was calculated within each group. This analysis tests whether stronger riverine sediment supply tends to decouple SSC from local wave resuspension at the global scale, or whether low- to moderate-supply coasts more often show strong positive wave–sediment coupling.

Assessment of wave bed shear stress changes and linked wetland load

We quantified ocean-side weakening of coastal wetland sediment-mobilization lifelines by linking nearshore changes in wave-induced bed shear stress to the wetland area potentially served by each coastal ocean cell. Coastal wetland distributions were taken from the GWL_FCS30D global 30 m annual wetland dataset, which was developed from Landsat time series, covers 2000–2022 and distinguishes eight wetland subcategories, including mangrove forest, salt marsh and tidal flat[46]. We used the 2022 layer and retained only these three coastal tidal wetland classes. The native 30 m wetland pixels were aggregated to a 0.10° global grid, with class-specific wetland area calculated from latitude-dependent spherical cell area and expressed in km².

Future changes in ocean-side wave forcing were represented as percentage changes in wave-induced bed shear stress relative to the present-day baseline. Sea-level forcing was taken from the IPCC AR6 sea-level projection dataset, which provides global and regional projections consistent with the Sixth Assessment Report, including relative sea-level projections[36,37,47]. We used the median relative sea-level projections with vertical land motion for SSP1-2.6, SSP2-4.5 and SSP5-8.5 in 2050 and 2100, with the main case defined as SSP5-8.5 in 2100. Wave climate was held fixed, so the analysis isolates the effect of sea-level-rise-driven water-depth increase on nearshore wave bed shear stress.

We analysed changes in wave-induced bed shear stress rather than resuspension potential itself. A strict estimate of resuspension potential requires comparison between the applied bed shear stress and the critical erosion threshold τ_{cr}, but τ_{cr} varies strongly with sediment texture, mud content, consolidation, water content, organic matter and biological stabilization. Applying a globally uniform τ_{cr} would therefore risk conflating sediment-property heterogeneity with hydrodynamic change. We instead used $\Delta\tau_{\mathrm{wave}}$ as a more robust hydrodynamic metric: it does not determine whether resuspension must

occur at a given site, but it directly quantifies how sea-level rise weakens the nearshore capacity of waves to disturb the seabed.

Potential ocean–wetland associations were represented by a distance-decay weight between nearshore ocean cells and nearby coastal wetlands. For each nearshore ocean cell $i$and wetland class k, the linked wetland load $L_{i,k}$was calculated as

$$L_{i,k} = \sum_{x \in k,\, d_{ix} \le D_{\max}} A_{x,k} \exp(-\frac{d_{ix}}{\lambda})$$

where $A_{x,k}$ is the area of wetland class k in receptor cell x, d_{ix} is the distance between ocean cell i and wetland cell x, λ is the e-folding distance and $D_{\max}$ is the maximum connection distance. The main analysis used $\lambda = 50$km and $D_{\max} = 150$km. We additionally tested $\lambda/D_{\max} = 25/100$, 50/150 and 100/300 km to evaluate sensitivity to the assumed spatial reach of ocean-to-wetland coupling. This linked load should not be interpreted as a measured sediment flux; rather, it provides a first-order global weight for the amount of coastal wetland area potentially connected to each nearshore sediment-mobilization cell.

Class-level shear-stress changes were summarized using the linked wetland load as the weighting factor. For each wetland class k, the weighted mean change in wave-induced bed shear stress was calculated as

$$\bar{\Delta\tau}_k = \frac{\sum_i L_{i,k}\, \Delta\tau_i}{\sum_i L_{i,k}}$$

where $\Delta\tau_i$ is the percentage change in wave-induced bed shear stress at nearshore ocean cell i. The fraction of wetland-linked load exposed to severe weakening was calculated as

$$F_k(25) = \frac{\sum_i L_{i,k}\, 1(\Delta\tau_i < -25\%)}{\sum_i L_{i,k}}$$

The 25% threshold was selected because it is comparable to the magnitude of wave-bed-shear-stress decline currently for the Louisiana nearshore shelf. It therefore provides both a regional physical reference and a conservative threshold for ecologically meaningful weakening. It is not a validated ecological threshold. This metric represents the proportion of wetland-connected ocean-side load associated with a decrease in wave bed shear stress larger than 25%, rather than a change calculated directly over land wetland pixels.

Stress-weighted wetland area combines fractional shear-stress decline with linked wetland area. For each wetland class, it was defined as

$$S_k = \frac{1}{100} \sum_i L_{i,k} \max(-\Delta\tau_i, 0)$$

Only declines in wave-induced bed shear stress contribute to stress-weighted wetland area; increasing stress contributes zero. Stress decreases are converted from percentages to fractions (for example, 0.30 for a 30% decline), giving units of km². Because receptors may contribute to multiple ocean cells, this sum represents repeated distance-weighted associations, not unique wetland area, sediment mass or predicted wetland loss. Absolute values depend on the ocean grid and kernel; scenario comparisons use the same grid. For scenario comparison, stress-weighted wetland area was normalized by the corresponding value in the main case.

The distribution of weakening was characterized with linked-load-weighted densities and exceedance curves. For each wetland class, the distribution of negative $\Delta\tau_i$ values was computed using $L_{i,k}$ as the weight. The exceedance curve was defined within the declining linked area as

$$E_k(x) = P(\Delta\tau_i < -x \mid k, \Delta\tau_i < 0) = \frac{\sum_i L_{i,k}\, 1(-\Delta\tau_i > x, \Delta\tau_i < 0)}{\sum_i L_{i,k}\, 1(\Delta\tau_i < 0)}$$

With this conditional definition, $E_k(0) = 100\%$, allowing the curves to compare the severity structure of already weakened ocean-side lifelines among mangroves, salt marshes and tidal flats.

A simple numerical example illustrates how the linked-load metrics operate and what they mean physically. Consider one nearshore ocean cell connected to two salt-marsh receptor cells: one has an area of 20 km² and lies 20 km away, while the other has an area of 10 km² and lies 100 km away. With the main kernel $\lambda = 50$ km, the salt-marsh linked load of this ocean cell is

$$20e^{-20/50} + 10e^{-100/50} = 14.76\ \text{km}^2$$

If this ocean cell has $\Delta\tau_{\text{wave}} = -30\%$, its contribution to salt-marsh stress-weighted wetland area is

$$14.76 \times 0.30 = 4.428\ \text{km}^2$$

If a second ocean cell has a salt-marsh linked load of 5 km² and $\Delta\tau_{\text{wave}} = -10\%$, the linked-load-weighted mean shear-stress change for salt marsh is

$$\frac{14.76(-30) + 5(-10)}{14.76 + 5} = -24.9\%.$$

In the same example, the fraction of salt-marsh linked load exposed to a $> 25\%$ decrease is $14.76/(14.76 + 5) = 74.7\%$, meaning that about three quarters of the declining salt-marsh-linked load is connected to ocean-side forcing that weakens by more than 25%. The stress-weighted wetland area is $14.76 \times 0.30 + 5 \times 0.10 = 4.928\ \text{km}^2$. Thus, the weighted mean measures the typical weakening magnitude, the severe-exposure fraction measures how much linked wetland area is connected to strongly weakened ocean-side forcing, and stress-weighted wetland area combines the magnitude of weakening with the amount of wetland area potentially affected.

Sensitivity analyses tested whether the inferred weakening depended on sea-level scenario or on the assumed spatial reach of the ocean-side lifeline. Scenario sensitivity was assessed by holding the main distance-decay kernel and wave statistic fixed, then comparing SSP1-2.6, SSP2-4.5 and SSP5-8.5 in 2050 and 2100 for three class-level metrics: weighted mean $\Delta\tau_{\mathrm{wave}}$, the fraction of linked wetland load exposed to $> 25\%$ shear-stress decrease and stress-weighted wetland area relative to the main case. Kernel sensitivity was assessed by recomputing the linked wetland load with $\lambda/D_{\max} = 25/100$, 50/150 and 100/300 km while keeping the same sea-level and wave-forcing case. Because this analysis changes only the spatial connection between ocean cells and wetland receptors, it isolates the robustness of the results to the assumed length scale of offshore-to-wetland coupling. The latitude restriction was tested by comparing the primary analysis (≤66°N) with the full domain (**Figure S16**).

References

1. Barbier, E. B. et al. The value of estuarine and coastal ecosystem services. Ecological Monographs 81, 169-193 (2011). https://doi.org/10.1890/10-1510.1

2. Mcleod, E. et al. A blueprint for blue carbon: toward an improved understanding of the role of vegetated coastal habitats in sequestering CO_2. Frontiers in Ecology and the Environment 9, 552-560 (2011). https://doi.org/10.1890/110004

3. Möller, I. et al. Wave attenuation over coastal salt marshes under storm surge conditions. Nature Geoscience 7, 727-731 (2014). https://doi.org/10.1038/ngeo2251

4. Morris, J. T., Sundareshwar, P. V., Nietch, C. T., Kjerfve, B. & Cahoon, D. R. Responses of coastal wetlands to rising sea level. Ecology 83, 2869-2877 (2002). https://doi.org/10.1890/0012-9658(2002)083[2869:ROCWTR]2.0.CO;2

5. Kirwan, M. L. & Megonigal, J. P. Tidal wetland stability in the face of human impacts and sea-level rise. Nature 504, 53-60 (2013). https://doi.org/10.1038/nature12856

6. Saintilan, N. et al. Constraints on the adjustment of tidal marshes to accelerating sea level rise. Science 377, 523-527 (2022). https://doi.org/10.1126/science.abo7872

7. Syvitski, J. P. M. et al. Impact of humans on the flux of terrestrial sediment to the global coastal ocean. Science 308, 376-380 (2005). https://doi.org/10.1126/science.1109454

8. Dethier, E. N., Renshaw, C. E. & Magilligan, F. J. Rapid changes to global river suspended sediment flux by humans. Science 376, 1447-1452 (2022). https://doi.org/10.1126/science.abn7980

9. Törnqvist, T. E. et al. Mississippi Delta subsidence primarily caused by compaction of Holocene strata. Nature Geoscience 1, 173-176 (2008). https://doi.org/10.1038/ngeo129

10. Jankowski, K. L., Törnqvist, T. E. & Fernandes, A. M. Vulnerability of Louisiana's coastal wetlands to present-day rates of relative sea-level rise. Nature Communications 8, 14792 (2017). https://doi.org/10.1038/ncomms14792

11. Ensign, S. H., Halls, J. N. & Peck, E. K. Watershed sediment cannot offset sea level rise in most US tidal wetlands. Science 382, 1191-1195 (2023). https://doi.org/10.1126/science.adj0513

12. Weston, N. B. Declining sediments and rising seas: an unfortunate convergence for tidal wetlands. Estuaries and Coasts 37, 1-23 (2014). https://doi.org/10.1007/s12237-013-9654-8

13. Fagherazzi, S. et al. Numerical models of salt marsh evolution: ecological, geomorphic, and climatic factors. Reviews of Geophysics 50, RG1002 (2012). https://doi.org/10.1029/2011RG000359

14. Green, M. O. & Coco, G. Review of wave-driven sediment resuspension and transport in estuaries. Reviews of Geophysics 52, 77-117 (2014). https://doi.org/10.1002/2013RG000437

15. Ganju, N. K. Marshes are the new beaches: integrating sediment transport into restoration planning. Estuaries and Coasts 42, 917-926 (2019). https://doi.org/10.1007/s12237-019-00531-3

16. Teng, W. et al. Marine-sourced sediment supply supports salt marsh resilience to sea level rise in the Northeastern US. Geophysical Research Letters 52, e2025GL118706 (2025). https://doi.org/10.1029/2025GL118706

17. Cortese, L., Zhang, X., Simard, M. & Fagherazzi, S. Storm impacts on mineral mass accumulation rates of coastal marshes. Journal of Geophysical Research: Earth Surface 129, e2023JF007065 (2024). https://doi.org/10.1029/2023JF007065

18. Georgiou, I. Y., FitzGerald, D. M., Sakib, M. M., Messina, F., Kulp, M. A. & Miner, M. D. Storm dynamics control sedimentation and shelf–bay–marsh sediment exchange along the Louisiana coast. Geophysical Research Letters 51, e2024GL111344 (2024). https://doi.org/10.1029/2024GL111344

19. Yang, S. L. et al. Role of delta-front erosion in sustaining salt marshes under sea-level rise and fluvial sediment decline. Limnology and Oceanography 65, 1990–2009 (2020). https://doi.org/10.1002/lno.11432

20. Schuerch, M., Spencer, T. & Evans, B. Coupling between tidal mudflats and salt marshes affects marsh morphology. Marine Geology 412, 95–106 (2019). https://doi.org/10.1016/j.margeo.2019.03.008

21. Castagno, K. A., Jiménez-Robles, A. M., Donnelly, J. P., Wiberg, P. L., Fenster, M. S. & Fagherazzi, S. Intense storms increase the stability of tidal bays. Geophysical Research Letters 45, 5491–5500 (2018). https://doi.org/10.1029/2018GL078208

22. Hopkinson, C. S., Morris, J. T., Fagherazzi, S., Wollheim, W. M. & Raymond, P. A. Lateral marsh edge erosion as a source of sediments for vertical marsh accretion. Journal of Geophysical Research: Biogeosciences 123, 2444-2465 (2018). https://doi.org/10.1029/2017JG004358

23. Mariotti, G. & Fagherazzi, S. Critical width of tidal flats triggers marsh collapse in the absence of sea-level rise. Proceedings of the National Academy of Sciences USA 110, 5353-5356 (2013). https://doi.org/10.1073/pnas.1219600110

24. Spencer, T. et al. Global coastal wetland change under sea-level rise and related stresses: the DIVA Wetland Change Model. Global and Planetary Change 139, 15-30 (2016). https://doi.org/10.1016/j.gloplacha.2015.12.018

25. Schuerch, M. et al. Future response of global coastal wetlands to sea-level rise. Nature 561, 231-234 (2018). https://doi.org/10.1038/s41586-018-0476-5

26. Kirwan, M. L., Temmerman, S., Skeehan, E. E., Guntenspergen, G. R. & Fagherazzi, S. Overestimation of marsh vulnerability to sea level rise. Nature Climate Change 6, 253–260 (2016). https://doi.org/10.1038/nclimate2909

27. Soulsby, R. Dynamics of Marine Sands: A Manual for Practical Applications. Thomas Telford (1997). https://doi.org/10.1680/doms.25844

28. Törnqvist, T. E. et al. Tipping points of Mississippi Delta marshes due to accelerated sea-level rise. Science Advances 6, eaaz5512 (2020). https://doi.org/10.1126/sciadv.aaz5512

29. Couvillion, B. R. et al. Land area change in coastal Louisiana (1932 to 2016). U.S. Geological Survey Scientific Investigations Map 3381 (2017). https://doi.org/10.3133/sim3381

30. Walker, N. D. & Hammack, A. B. Impacts of winter storms on circulation and sediment transport: Atchafalaya-Vermilion Bay region, Louisiana, U.S.A. Journal of Coastal Research 16, 996–1010 (2000). https://repository.lsu.edu/oceanography_coastal_pubs/1308/

31. Wahl, T., Calafat, F. M. & Luther, M. E. Rapid changes in the seasonal sea level cycle along the US Gulf coast from the late 20th century. Geophysical Research Letters 41, 491–498 (2014). https://doi.org/10.1002/2013GL058777

32. Lo, E. L., Bentley, S. J. & Xu, K. Experimental study of cohesive sediment consolidation and resuspension identifies approaches for coastal restoration: Lake Lery, Louisiana. Geo-Marine Letters 34, 499–509 (2014). https://doi.org/10.1007/s00367-014-0381-3

33. Tolhurst, T. J., Gust, G. & Paterson, D. M. The influence of an extracellular polymeric substance (EPS) on cohesive sediment stability. In Fine Sediment Dynamics in the Marine Environment (eds Winterwerp, J. C. & Kranenburg, C.) 409–425 (Elsevier, 2002). https://doi.org/10.1016/S1568-2692(02)80030-4

34. Stanley, D. J. & Warne, A. G. Nile Delta in its destruction phase. Journal of Coastal Research 14, 794-825 (1998). https://research.si.edu/publication-details/?id=59596

35. Anthony, E. J., Besset, M., Zainescu, F. & Goichot, M. Geomorphology of a tropical river delta under pressure: the Rufiji delta, Tanzania—context, channel connectivity and alongshore morpho-sedimentary and hydrodynamic variability. Geo-Marine Letters 41, 24 (2021). https://doi.org/10.1007/s00367-021-00695-7

36. Fox-Kemper, B. et al. Ocean, cryosphere and sea level change. In Climate Change 2021: The Physical Science Basis. Contribution of Working Group I to the Sixth Assessment Report of the Intergovernmental Panel on Climate Change 1211–1362 (Cambridge Univ. Press, 2021). https://doi.org/10.1017/9781009157896.011

37. Garner, G. G. et al. IPCC AR6 Sea Level Projections. Version 20210809. Zenodo (2021). https://doi.org/10.5281/zenodo.6382554

38. Wells, S., Henderson, B., Dansie, A., Friess, D. A., Balke, T. & Glamore, W. Global mangrove distribution on the open coast is controlled by waves. Nature (2026). https://doi.org/10.1038/s41586-026-11089-z

39. Harringmeyer, J. P., Ghosh, N., Weiser, M. W., Thompson, D. R., Simard, M., Lohrenz, S. E., & Fichot, C. G. (2024). A hyperspectral view of the nearshore Mississippi River Delta: Characterizing suspended particles in coastal wetlands using imaging

spectroscopy. Remote Sensing of Environment, 301, 113943. https://doi.org/10.1016/j.rse.2023.113943

40. Nechad, B., Ruddick, K. G. & Park, Y. Calibration and validation of a generic multisensor algorithm for mapping of total suspended matter in turbid waters. Remote Sensing of Environment 114, 854–866 (2010). https://doi.org/10.1016/j.rse.2009.11.022

41. Sathyendranath, S. et al. An ocean-colour time series for use in climate studies: the experience of the Ocean-Colour Climate Change Initiative (OC-CCI). Sensors 19, 4285 (2019). https://doi.org/10.3390/s19194285

42. Hersbach, H. et al. The ERA5 global reanalysis. Quarterly Journal of the Royal Meteorological Society 146, 1999-2049 (2020). https://doi.org/10.1002/qj.3803

43. Hirsch, R. M., Moyer, D. L. & Archfield, S. A. Weighted regressions on time, discharge, and season (WRTDS), with an application to Chesapeake Bay river inputs. Journal of the American Water Resources Association 46, 857–880 (2010). https://doi.org/10.1111/j.1752-1688.2010.00482.x

44. Campbell, A. D., Fatoyinbo, L., Goldberg, L. & Lagomasino, D. Global hotspots of salt marsh change and carbon emissions. Nature 612, 701–706 (2022). https://doi.org/10.1038/s41586-022-05355-z

45. Maritorena, S., Hembise Fanton d'Andon, O., Mangin, A. & Siegel, D. A. Merged satellite ocean color data products using a bio-optical model: characteristics, benefits and issues. Remote Sensing of Environment 114, 1791-1804 (2010). https://doi.org/10.1016/j.rse.2010.04.002

46. Zhang, X. et al. Global annual wetland dataset at 30 m with a fine classification system from 2000 to 2022. Scientific Data 11, 310 (2024). https://doi.org/10.1038/s41597-024-03143-0

47. Kopp, R. E. et al. The Framework for Assessing Changes To Sea-level (FACTS) v1.0: a platform for characterizing parametric and structural uncertainty in future global, relative, and extreme sea-level change. Geoscientific Model Development 16, 7461–7489 (2023). https://doi.org/10.5194/gmd-16-7461-2023

Acknowledgments

Funding: This work was primarily supported by National Aeronautics and Space Administration (NASA) Grant 80NSSC23K0129, under the Earth System Science for Building Coastal Resilience program (NNH22ZDA001N-COASTAL), and the Future in NASA Earth and Space Science and Technology (FINESST) Grant 80NSSC25K0459 (FI Lin, PI Fichot). Partial support was also provided by the U.S. National Science Foundation Award 2224608 (PIE LTER).

Author contributions: Conceptualization: H.L., C.F., and S.F. Methodology: H.L. and S.J. Formal analysis: H.L., S.J., and C.F. Investigation: H.L., C.F., and S.F. Data curation: H.L. Validation: H.L. Visualization: H.L. Funding acquisition: H.L., C.F., and S.F. Resources: C.F. and S.F. Project administration: C.F. and S.F. Supervision: H.L., C.F., and S.F. Writing—original draft: H.L. Writing—review and editing: H.L., S.J., C.F., and S.F.

Competing interests: The authors declare no competing interests.

Data, code, and materials availability: Public datasets used in this study are available from the following sources: **Ocean Colour CCI** satellite reflectance data: https://climate.esa.int/en/projects/ocean-colour/data/**; Copernicus GlobColour** suspended particulate matter data: https://data.marine.copernicus.eu/product/OCEANCOLOUR_GLO_BGC_L3_MY_009_103/description; **ERA5** wind and wave reanalysis: https://cds.climate.copernicus.eu/datasets/reanalysis-era5-single-levels; **NOAA CO-OPS** coastal water-level observations: https://tidesandcurrents.noaa.gov/; **Coastal water-level and river sediment data:** Coastal water-level observations from Grand Isle (8761724), Port Fourchon (8762075), and Pilots Station (8760922) are available from NOAA CO-OPS (https://tidesandcurrents.noaa.gov/). WRTDS-derived sediment loads for the Mississippi River at St. Francisville and the Atchafalaya River at Melville are available from the USGS (https://doi.org/10.5066/P1MFARP2); **Louisiana Coastwide Reference Monitoring System (CRMS)** marsh elevation and accretion data: https://www.lacoast.gov/crms/; **Global Salt Marsh Change (2000–2019)**: https://doi.org/10.3334/ORNLDAAC/2122; **GWL_FCS30D** global wetland distribution data: https://doi.org/10.5281/zenodo.10068479; **IPCC AR6** regional sea-level projections: https://doi.org/10.5281/zenodo.6382554; **Global river sediment flux** data: https://doi.org/10.5281/zenodo.7808492
Analysis code is publicly available at https://github.com/HangjieLin/offshore-sediment-lifeline.

Supplementary Files

This is a list of supplementary files associated with this preprint. Click to download.

- supportinginformation.docx